Phase equilibria at Si-HfO$_2$ and Pt-HfO$_2$ interfaces from first principles thermodynamics

H. Zhu, C. Tang,[*] and R. Ramprasad[†]

Department of Chemical, Materials and Biomolecular Engineering, Institute of Materials Science,
University of Connecticut, 97 North Eagleville Road, Storrs, Connecticut 06269, USA

The phase diagrams of Si-HfO$_2$ and Pt-HfO$_2$ interfaces as a function of temperature and oxygen pressure have been determined using first principles thermodynamics (FPTs), i.e., by combining conventional density-functional theory results with thermodynamics. The vibrational and configurational entropic contributions to the free energies of the condensed phases are explicitly included in this treatment. We demonstrate that the predictions of the FPT approach are in quantitative agreement with experiments for the classes of interfaces considered here. In particular, under ultrahigh vacuum (UHV) conditions, we show that FPT methods predict the correct Si-HfO$_2$ silicalike interface configurations. Likewise, we also show that an interfacial oxygen coverage of 0.5–1.0 monolayer is favored under UHV conditions at the Pt-HfO$_2$ interface before rapid oxidation of Pt may be expected (for higher oxygen pressures). These results have important implications both for the applicability of FPT methods for the considered classes of interfaces as well as for "high-K" dielectrics-based electronic devices in which such interfaces are expected.

I. INTRODUCTION

The determination of the surface and interface phase diagrams when systems are in equilibrium with appropriate gas phase molecules using first principles thermodynamics (FPTs) constitutes a reasonably mature computational methodology in materials research. FPT has been successfully used to study a diversity of systems, situations and applications,[1–4] most notably phenomena encountered in catalysis.[1,2] These calculations typically involve zero-temperature density-functional theory (DFT) determinations of the energies (i.e., the internal energy or enthalpy), a statistical mechanical treatment of the free energy of the gas phase within the ideal gas approximation, and occasionally, normal-mode analyses (to capture the vibrational entropic contribution to the free energy of the condensed phases). This framework has thus enabled a "bridging" of the zero-temperature results of traditional DFT calculations to practical situations involving nonzero temperatures and pressures.

The present work attempts to use the FPT methodology to study two types of interfaces found in an emerging technologically important structure, namely, metal-oxide-Si field-effect transistors (MOSFETs) based on high dielectric constant (or "high-K") oxides.[5,6] Driven by requirements for device miniaturization, the semiconductor industry is poised to replace the pervasive SiO$_2$ dielectric with an HfO$_2$-based high-K oxide in MOSFETs. This alteration also requires the replacement of the erstwhile poly-Si based gate electrode by one that is based on metals with appropriate work functions. This emerging "gate stack" structure will thus have two new interfaces (relative to the SiO$_2$-based MOSFETs), namely, the Si-HfO$_2$ and HfO$_2$-metal interfaces, each of which brings along a different set of challenges.

While it appears that the formation of an SiO$_x$ phase at the Si-HfO$_2$ interface is inevitable under normal processing conditions, controlling and maintaining the thickness of this interfacial layer is critical.[7,8] Large SiO$_x$ thicknesses will lead to a reduction in the overall dielectric constant of the dielectric layer (thereby negating the benefits of using a high-K dielectric); on the other hand, the elimination of the SiO$_x$ layer may result in the formation of Hf-Si bonds, and hence, silicides which are metallic.[5] In fact, reversible formation of SiO$_x$ and silicides at the Si-HfO$_2$ interface by annealing in oxygen-rich and oxygen-deficient environments, respectively, have been observed previously.[9,10] First principles studies on HfO$_2$-based gate stacks have provided some insights into these interface phenomena. A series of calculations[11–15] on Si-HfO$_2$ interfaces have indicated that point defects, such as O vacancies and interstitials, prefer to segregate to the interfaces, regardless of the phase of HfO$_2$. The driving force for such segregations is provided by the lower formation and migration barrier energies in the vicinity of the interfaces than in bulk HfO$_2$. Since such zero-temperature DFT calculations do not make particular reference to the temperature and pressure-dependent chemical potentials of the oxygen ambient, the results of these computations cannot be directly related to processing conditions, e.g., annealing.

The metal-HfO$_2$ interface presents a separate set of issues although these too are related to the interface morphology and defect chemistry. While one desires to utilize metal electrodes with appropriate work functions such that the metal Fermi level lines up with either the valence- or conduction-band edge of the underlying Si substrate, the interfacial chemistries (in terms of charge transfer, bond formation, defect accumulation, dipole creation, etc.) lead to shifts in the work function value from its true vacuum value.[16–21]

Thus, in both cases of Si-HfO$_2$ and metal-HfO$_2$ interfaces, it would be valuable to understand the relationship between ambient conditions (e.g., temperature and oxygen pressure) and interface morphologies. Furthermore, it would be important to assess the level of accuracy that may be expected when one uses FPT to arrive at such relationships, especially when one is forced to make inevitable approximations of the atomic-level structure in such computational treatments. Here, for definiteness, we choose Pt as the metal electrode, and present phase diagrams for Si-HfO$_2$ and Pt-HfO$_2$ inter-

TABLE I. Calculated lattice parameters (Å) for m-HfO$_2$, Si, and Pt. The results based on Vanderbilt ultrasoft pseudopotentials and projector-augmented wave approach are labeled by "us" and "paw," respectively. The corresponding experimental values are indicated in parentheses.

	m-HfO$_2$	Si	Pt
a	5.14^{us}, 5.09^{paw} (5.12[a])	5.46^{us} (5.43[b])	3.98^{paw} (3.92[c])
b	5.19^{us}, 5.14^{paw} (5.17[a])		
c	5.30^{us}, 5.27^{paw} (5.29[a])		

[a]Reference 27.
[b]Reference 28.
[c]Reference 29.

faces as a function of temperature and oxygen pressure. Our results are consistent with available experimental data and are indicative of the predictive nature of such first principles structure-process(-property) relationship studies.

This paper is organized as follows. In Sec. II, we discuss the methods adopted to calculate the phase diagrams, including the details of DFT calculations, the interface models, and the FPT methodology. In Sec. III, we present our zero-temperature DFT results and interface phase diagrams obtained using FPT. Through explicit inclusion of the vibrational and configurational entropic contributions in the free energies of the condensed phases, we provide an estimate of errors introduced due to the neglect of these terms. We also comment on the impact of the spurious strains inherent in supercell treatments of heterostructures. Section IV summaries our conclusions. The Appendix contrasts different approaches for calculating the oxygen chemical potential adopted widely in prior FPT studies.

II. METHODS

A. DFT calculations and models

Our DFT calculations were performed using the VASP code[22] with the PW91 generalized gradient approximation[23]

and a cut-off energy of 400 eV for the plane-wave expansion of the wave functions. Vanderbilt ultrasoft pseudopotentials[24] and projector-augmented wave approach[25] are applied to Si-HfO$_2$ and Pt-HfO$_2$ interface calculations, respectively, with HfO$_2$ in the monoclinic phase. Amorphous HfO$_2$ (a-HfO$_2$) is not considered in this work considering the difficulty to unambiguously define the O coverage at the interface between a-HfO$_2$ and Si or Pt. We note that such difficulties arise in the definition of point defects even in bulk a-HfO$_2$.[26] Monkhorst-Pack k-point meshes of $5 \times 5 \times 5$, $5 \times 5 \times 5$, and $11 \times 11 \times 11$, respectively, were used in the case of bulk m-HfO$_2$, Si, and Pt. In the case of heterostructures discussed below, the mesh indices were decreased in proportion to the unit-cell dimensions. As shown in Table I, the calculated equilibrium lattice parameters of the bulk systems are in good agreement with experimental values.

Our interface models were constructed in a supercell that consists of an X-HfO$_2$ (X=Si or Pt) heterostructure and a vacuum of about 10 Å (Fig. 1). All atoms were allowed to relax to their equilibrium positions until every component of each atomic force was smaller than 0.04 eV/Å. Dipole corrections were used to handle the asymmetric nature of the heterostructures considered. The interface morphologies were modeled by varying the concentration of O at the X-HfO$_2$ interface. The corresponding interface configurations are represented by X:θ_O:HfO$_2$, where θ_O stands for the fractional monolayer (ML) interfacial O coverage. In keeping with the stoichiometry of HfO$_2$, an ML is defined as two times the number of Hf atoms in a layer.

The Si-HfO$_2$ interface model was constructed by coherently placing a stretched (001) (1×1) m-HfO$_2$ slab on a (001) (1×1) Si slab [Fig. 1(a)], as has been done before.[12,13] This is expected to represent the situation in which Si is the substrate (and hence displays its optimal lattice parameter) while HfO$_2$ conforms to match Si. Such a constraint causes 6% and 5% strains in the HfO$_2$ slab along the a and b directions. The Si side of the heterostructure is composed of two-atom Si layers, and the HfO$_2$ side consists of alternating
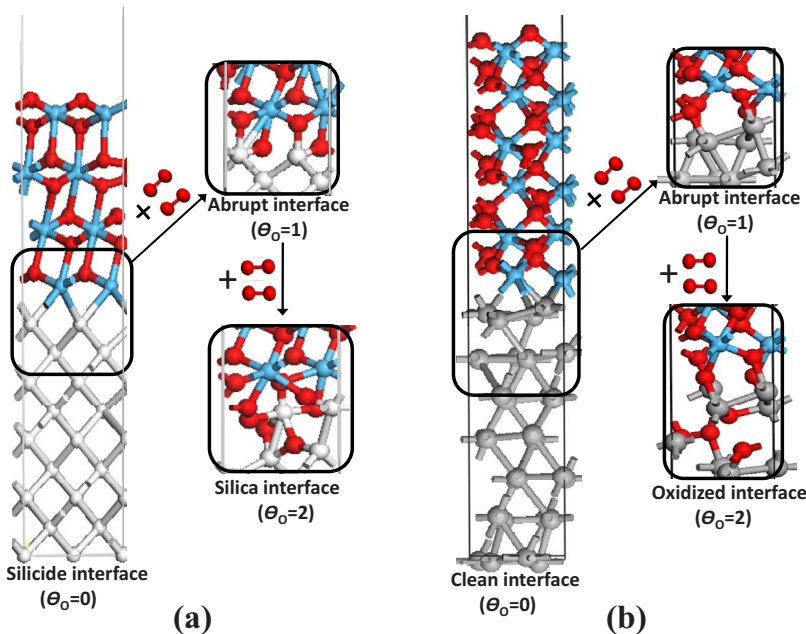

FIG. 1. (Color online) The representative atomic structures of the X-HfO$_2$ heterostructures with X at the bottom: (a) Si-HfO$_2$ interface and (b) Pt-HfO$_2$ interface. The Hf and O atoms of the top HfO$_2$ parts in both (a) and (b) are represented by light blue (gray) and red (dark) spheres, respectively.

two-atom Hf layers and four-atom O bilayers (with each sublayer of the bilayer containing two O atoms). The HfO$_2$ free surface was always passivated by termination with half of an O bilayer. A well-passivated Si-HfO$_2$ interface requires a complete O bilayer, with one sublayer passivating HfO$_2$ and the other passivating Si.[30] We refer to this situation as an "abrupt" interface, and as per our definition of ML, $\theta_O = 1$ for this case. $\theta_O = 0$ corresponds to an interface completely depleted of O, and is thus composed of primarily Hf-Si bonds; we refer to this as a "silicide" interface. $\theta_O > 1$ represents a situation in which O atoms in excess of 1 ML prefer to penetrate the Si side of the heterostructure, with the most favorable sites being between the top two Si layers;[12] we refer to this as an "oxidized" interface. The interfacial O coverage considered in this work ranges from 0 to 2 ML in steps of 0.25 ML. Figure 1(a) shows three representative interface structures, namely, the silicide ($\theta_O = 0$), abrupt ($\theta_O = 1$), and silica ($\theta_O = 2$) interfaces.

Following recent work by Gavrikov *et al.*,[31] we constructed the Pt-HfO$_2$ interface by matching a strained (111) ($2 \times \sqrt{3}$) Pt slab to a (001) (1×1) m-HfO$_2$ slab [Fig. 1(b)], which results in -9% and 5% strains in Pt along the a and b directions of HfO$_2$. Such a strained situation is appropriate as Pt is deposited on a HfO$_2$ film in practice and one expects Pt to conform to HfO$_2$. This heterostructure is composed of four-atom Pt layers, two-atom Hf layers, and four-atom O bilayers. Interfacial O coverage was treated in the same manner as in the Si-HfO$_2$ case, i.e., ranging from 0 to 2 ML in steps of 0.25 ML. For $\theta_O = 0$, the interface is represented by Pt-Hf bonding. For $\theta_O = 1$, one half of the interfacial O bilayer atoms (i.e., all of one O sublayer atoms) passivates the interfacial Hf atoms and the other half bonds to interfacial Pt atoms. For $\theta_O > 1$, the extra O atoms sit between the two Pt layers next to the interface. As shown in Fig. 1(b), the local structure of Pt-O bonding at the Pt:2:HfO$_2$ interface (i.e., $\theta_O = 2$) mimics a distorted platinum oxide. To be specific, the Pt:0:HfO$_2$, Pt:1:HfO$_2$, and Pt:2:HfO$_2$ interfaces are referred to as "clean," abrupt, and oxidized interfaces, respectively.

We now comment about our specific choices for the orientation of HfO$_2$, Si, and Pt subsystems, which were guided by the requirement of least strain for a supercell size that may be practically considered. Coherently placing the most stable surfaces of Si and Pt [namely, (001) and (111), respectively] on (001) HfO$_2$ resulted in strains of less than 9%, as described above. However, matching the most stable surface of HfO$_2$, namely ($\bar{1}11$), on (001) Si or (111) Pt with a computational executable supercell size involved significantly larger strains. For example, if we stretch (111) (2×3) Pt to match ($\bar{1}11$) (1×1) HfO$_2$, the strain would be 14% and 19% along a and b axes of the interface plane. These considerations have lead to the current choices of orientations.

In order to assess the impact of the existing strain in our chosen orientations on the final results, a limited number of "counterstrain" calculations (for $\theta_O = 0$, 0.5, and 1) were also performed. In these calculations, Si was strained to match HfO$_2$ in the Si-HfO$_2$ heterostructure case and HfO$_2$ was strained to match Pt in the Pt-HfO$_2$ heterostructure case. These results are discussed in Sec. III.

B. Thermodynamics

We now describe the approach used to create the interface phase diagrams based on FPT. The most stable interface is the one with minimum interface free energy (γ_{θ_O}), which can be defined as

$$\gamma_{\theta_O} = (G_{\theta_O} - n_{Hf}\mu_{Hf} - n_O\mu_O - n_X\mu_X)/A - \sigma_{HfO_2} - \sigma_X, \quad (1)$$

where G_{θ_O} is the Gibbs free energy for the $X:\theta_O:$HfO$_2$ heterostructure, A is the interface area, and n_{Hf}, n_O, and n_X are, respectively, the number of Hf, O, and X atoms in the heterostructure. μ_{Hf} and μ_O are the chemical potentials of Hf and O in bulk m-HfO$_2$ and μ_X is the chemical potential of X in its stable elemental form, which is the diamond cubic structure for Si and the face-centered-cubic structure for Pt. σ_{HfO_2} and σ_X are the surface energies of the two free surfaces. Note that the surface-energy terms are insensitive to the interface structures and will drop out when relative interface energies are considered (as done below).

Moreover, the chemical potentials in the above equation satisfy the following relationships:

$$\mu_{Hf} + 2\mu_O = G_{HfO_2},$$

$$\mu_X = G_X, \quad (2)$$

where G_{HfO_2} and G_X are the Gibbs free energies for bulk m-HfO$_2$ and bulk X, respectively. Substituting Eq. (2) into Eq. (1) results in

$$\gamma_{\theta_O} = [G_{\theta_O} - n_{Hf}G_{HfO_2} - (n_O - 2n_{Hf})\mu_O - n_X G_X]/A - \sigma_{HfO_2} - \sigma_X. \quad (3)$$

When $\theta_O = 0.5$, the whole system is stoichiometric ($n_{Hf}:n_O = 1:2$) and the interface energy is

$$\gamma_{0.5} = (G_{0.5} - n_{Hf}G_{HfO_2} - n_X G_X)/A - \sigma_{HfO_2} - \sigma_X. \quad (4)$$

By using $\gamma_{0.5}$ as a reference and replacing $n_O - 2n_{Hf}$ by $4 \times (\theta_O - 0.5)$ (4 accounts for the fact that 1 ML of O contains four atoms in the interfaces considered here), we can further define the relative interface energy as

$$\Delta\gamma_{\theta_O} = \gamma_{\theta_O} - \gamma_{0.5} = [G_{\theta_O} - G_{0.5} - 4(\theta_O - 0.5)\mu_O]/A. \quad (5)$$

This relative interface energy determines the stability of various interface structures and in turn the interface phase diagram.

In Eq. (5), the Gibbs free energy terms can be written as

$$G_{\theta_O} = E_{\theta_O}^{DFT} + \Delta H_{\theta_O}(T,P) + F_{\theta_O}^v + F_{\theta_O}^c + PV, \quad (6)$$

where $E_{\theta_O}^{DFT}$ denotes the DFT energy of the corresponding heterostructure, $\Delta H_{\theta_O}(T,P)$ is the enthalpy increase with temperature T and pressure P, and V is the volume. $F_{\theta_O}^v$ and $F_{\theta_O}^c$ are the vibrational and configurational energies, respectively. Substituting Eq. (6) into Eq. (5) and assuming $\Delta H_{\theta_O}(T,P)$ and PV for $X:\theta_O:$HfO$_2$ and $X:0.5:$HfO$_2$ are roughly equivalent (and hence can be canceled), we obtain the relative interface energy as

$$\Delta\gamma_{\theta_O} = [E^{DFT}_{\theta_O} - E^{DFT}_{0.5} + F^v_{\theta_O} - F^v_{0.5} + F^c_{\theta_O} - F^c_{0.5}$$
$$- 4(\theta_O - 0.5)\mu_O]/A. \tag{7}$$

The $X{:}\theta_O{:}HfO_2$ heterostructure reaches its equilibrium state at a certain temperature and oxygen pressure by exchanging O atoms with the surrounding atmosphere. Hence, μ_O in Eq. (7) could be replaced with one half of the chemical potential of an oxygen molecule, μ_{O_2}, which is a function of temperature (T) and oxygen pressure (P_{O_2}),

$$\mu_{O_2}(T, P_{O_2}) = E^{DFT}_{O_2} + \Delta\mu_{O_2}(T, P_{O_2}), \tag{8}$$

where $E^{DFT}_{O_2}$ is the DFT energy of an isolated O_2 molecule and $\Delta\mu_{O_2}(T, P_{O_2})$ contains the zero-point vibrational energy ($E^{ZPE}_{O_2}$) and the T and P dependence of chemical potential (see the Appendix). Hence, Eq. (7) could be written as

$$\Delta\gamma_{\theta_O} = \{E^{DFT}_{\theta_O} - E^{DFT}_{0.5} + F^v_{\theta_O} - F^v_{0.5} + F^c_{\theta_O} - F^c_{0.5} - (2\theta_O - 1)$$
$$\times [E^{DFT}_{O_2} + \Delta\mu_{O_2}(T, P_{O_2})]\}/A$$
$$= [\Delta E^{DFT}_{\theta_O} + \Delta F^v_{\theta_O} + \Delta F^c_{\theta_O} - (2\theta_O - 1)\Delta\mu_{O_2}(T, P_{O_2})]/A, \tag{9}$$

where $\Delta E^{DFT}_{\theta_O}$ stands for the DFT energy difference between $X{:}\theta_O{:}HfO_2$ and $X{:}0.5{:}HfO_2 + (2\theta_O - 1)O_2$, i.e., $\Delta E^{DFT}_{\theta_O} = E^{DFT}_{\theta_O} - E^{DFT}_{0.5} - (2\theta_O - 1)E^{DFT}_{O_2}$ and may be obtained from normal DFT calculations. Also, $\Delta F^v_{\theta_O} = F^v_{\theta_O} - F^v_{0.5}$ and $\Delta F^c_{\theta_O} = F^c_{\theta_O} - F^c_{0.5}$. Details on how $\Delta F^v_{\theta_O}$ and $\Delta F^c_{\theta_O}$ are estimated in the present work are provided in Sec. III C. Prior FPT works on the surface phase stabilities illustrate that $\Delta F^v_{\theta_O}$ and $\Delta F^c_{\theta_O}$ will not qualitatively affect the phase diagram although phase transition regions may be smoothed in the presence of these two terms.[32,33] Thus, in many treatments, $\Delta F^v_{\theta_O}$ and $\Delta F^c_{\theta_O}$ are dropped out in the computation of surface phase diagram. In such cases, $\Delta\gamma_{\theta_O}$ is purely a function of $\Delta E^{DFT}_{\theta_O}$ and $\Delta\mu_{O_2}(T, P_{O_2})$ (referred to here as $\Delta\gamma^{DFT}_{\theta_O}$),

$$\Delta\gamma^{DFT}_{\theta_O} = [\Delta E^{DFT}_{\theta_O} - (2\theta_O - 1)\Delta\mu_{O_2}(T, P_{O_2})]/A. \tag{10}$$

Equation (9) or (10) forms the basis for the construction of interface phase diagrams, from which one can compute the interface energy for various interface structures for given (T, P_{O_2}) combinations. The interface phase diagram is then obtained by identifying the most stable (i.e., minimum energy) interface as a function of T and P_{O_2}. In the present work, we use both Eqs. (9) and (10) to compute the phase diagrams to directly understand the impact of including $\Delta F^v_{\theta_O}$ and $\Delta F^c_{\theta_O}$.

III. RESULTS

A. DFT energies of X-HfO$_2$ heterostructures

The calculated $\Delta E^{DFT}_{\theta_O}$ for θ_O between 0 and 2 is shown in Fig. 2. Open symbols represent the situation when the substrate (Si in Si-HfO$_2$ interfaces and HfO$_2$ in Pt-HfO$_2$ interfaces) is at equilibrium but the overlayer is strained to con-

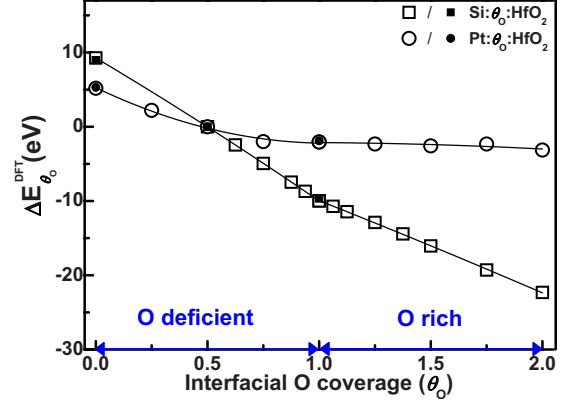FIG. 2. (Color online) DFT energy difference between $X{:}\theta_O{:}HfO_2$ and $X{:}0.5{:}HfO_2 + (2\theta_O - 1)O_2$, $\Delta E^{DFT}_{\theta_O}$. Open and solid squares stand for $\Delta E^{DFT}_{\theta_O}$ of Si-HfO$_2$ with HfO$_2$ under strain and Si under strain, respectively. Open and solid circles are the corresponding data for Pt-HfO$_2$ with Pt under strain and HfO$_2$ under strain, respectively.

form to the substrate. The corresponding results for a few counterstrained situations studied (i.e., when the substrate is strained to match the overlayer lattice parameters) are shown using solid symbols. It can be seen from Fig. 2 that the two different strain conditions display almost identical $\Delta E^{DFT}_{\theta_O}$ for the few cases considered. It can thus be safely concluded that although a certain amount of strain is introduced to maintain the interface coherency, $\Delta E^{DFT}_{\theta_O}$ (and, consequently, $\Delta\gamma^{DFT}_{\theta_O}$ and the phase diagrams) is largely unaffected due to the presence of strain.

To further explore interfacial configurations intermediate to the ones explicitly considered here, the DFT results were fitted using polynomial functions. As Fig. 2 shows, $\Delta E^{DFT}_{\theta_O}$ for the Si${:}\theta_O{:}HfO_2$ heterostructure changes almost linearly with the addition of O into the interface but with different slopes for $0 < \theta_O < 1$ and $1 < \theta_O < 2$. For Pt${:}\theta_O{:}HfO_2$ both linear ($\theta_O > 1$) and nonlinear ($0 < \theta_O < 1$) behaviors were observed. This linear or nonlinear dependence of $\Delta E^{DFT}_{\theta_O}$ on θ_O determines the smoothness of the transition from 1 ML to another, as will be discussed below.

B. Interface phase diagrams not including vibrational and configurational energies

We consider the interfaces first with the assumption that the contribution to the interface energy due to $\Delta F^v_{\theta_O}$ and $\Delta F^c_{\theta_O}$ may be ignored. This situation is described by Eq. (10). The advantage with considering this equation is that all T and P_{O_2} dependence of $\Delta\gamma^{DFT}_{\theta_O}$ is contained solely within $\Delta\mu_{O_2}$. Thus, as shown in Fig. 3, a plot of $\Delta\gamma^{DFT}_{\theta_O}$ versus $\Delta\mu_{O_2}$ yields straight lines, with the slope and intercept depending, respectively, on the interfacial O content and the value of $\Delta E^{DFT}_{\theta_O}$. The lower boundary of $\Delta\mu_{O_2}$ is confined to avoid the segregation of Hf from bulk HfO$_2$. Values of θ_O ranging from 0 to 2 in steps of 0.05 ML were considered (facilitated by the analytic fits obtained via Fig. 2). Lines corresponding to each value of θ_O are shown and the lowest energy inter-
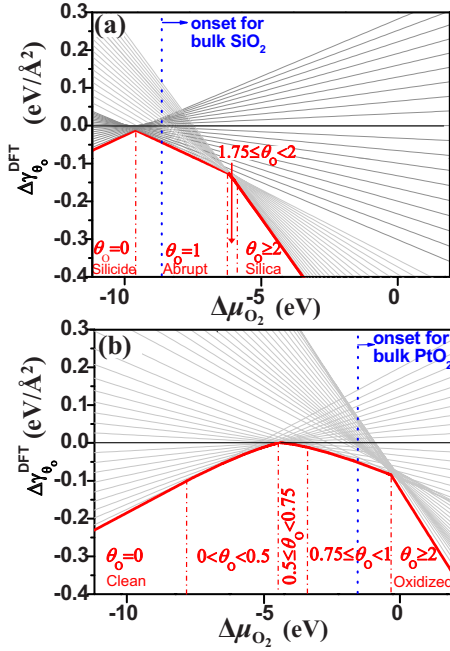
FIG. 3. (Color online) The relative interface free energy as a function of $\Delta\mu_{O_2}$ for the (a) Si-HfO$_2$ and (b) Pt-HfO$_2$ interfaces. The inner boundaries represent the lowest interface energy at each $\Delta\mu_{O_2}$ value. The corresponding θ_O value is indicated in the figure. The vertical dashed-dotted lines are boundaries between two different stable interface structures. The onset $\Delta\mu_{O_2}$ to form bulk SiO$_2$ and α-PtO$_2$ is indicated by the vertical dotted line in (a) and (b), respectively.

face at each $\Delta\mu_{O_2}$ value is identified along with the corresponding θ_O value. The critical $\Delta\mu_{O_2}$ value above which formation of the bulk XO$_2$ oxides is also indicated. At this critical $\Delta\mu_{O_2}$, bulk X is in equilibrium with bulk XO$_2$. Thus, the critical $\Delta\mu_{O_2}$ is given by $E_{XO_2} - E_X$, where E_X and E_{XO_2} are the DFT energies of X and XO$_2$ in their stable forms, namely, the hexagonal, monoclinic, face-centered-cubic, and α-PtO$_2$ structures, respectively, for bulk Hf, HfO$_2$, Pt, and PtO$_2$.

As shown in Fig. 3(a), the stable interface type in Si:θ_O:HfO$_2$ heterostructure changes abruptly from $\theta_O = 0$ to $\theta_O = 1$ at $\Delta\mu_{O_2} \sim -9.6$ eV and then to $\theta_O = 1.75$ at $\Delta\mu_{O_2} \sim -6.2$ eV. Nevertheless, when $2 > \theta_O > 1.75$, the interface changes smoothly. Moreover, bulk SiO$_2$ is favored at smaller $\Delta\mu_{O_2}$ values than interfacial silica. This is probably due to the fact that the oxidation of interfacial silicon is accompanied with strain and hence requires more energy. The Pt:θ_O:HfO$_2$ interface [shown in Fig. 3(b)], however, changes more smoothly for $\theta_O \leq 1$, and then abruptly changes from $\theta_O \sim 1$ to $\theta_O = 2$ at $\Delta\mu_{O_2} \sim -0.3$ eV. Similar to the Si-HfO$_2$ case (and presumably for the same reason), the critical $\Delta\mu_{O_2}$ for an oxidized Pt-HfO$_2$ interface is larger than the value (-1.45 eV) to form bulk PtO$_2$. As alluded to earlier, linearity of $\Delta E_{\theta_O}^{DFT}$ versus θ_O (cf. Fig. 2) correlates with abrupt transitions between stable interface O coverages. We note that while some aspects of the Pt:θ_O:HfO$_2$ as a function of $\Delta\mu_{O_2}$ have been presented earlier,[31] the present investigation constitutes a more detailed analysis of this interface (and is in agreement with the prior work).

Since $\Delta\mu_{O_2}$ is a function of T and P_{O_2}, the information contained in Fig. 3 may be used to create (T, P_{O_2}) phase diagrams in which each $\Delta\mu_{O_2}$ "turning point" of Fig. 3 becomes a curve in a T versus P_{O_2} plot, demarcating boundaries between two different phases. Such phase diagrams are presented in Figs. 4(a) and 5(a) for Si-HfO$_2$ and Pt-HfO$_2$ interfaces, respectively, under the assumption that $\Delta F_{\theta_O}^v$ and $\Delta F_{\theta_O}^c$ may be ignored.

From Fig. 4(a), we find that (not surprisingly) the interfacial silica phase prefers high oxygen pressure and low temperature while the silicide phase is stable at low oxygen pressure and high temperature. It is however interesting to note that interfacial silica can occur even at ultrahigh vacuum (UHV) condition ($P_{O_2} < 10^{-12}$ atm) in a wide temperature range, which explains why the interfacial silica phase is widely observed. The open and solid circles in Fig. 4(a), respectively, represent experimental conditions at which SiO$_2$ and SiO at Si-HfO$_2$ interfaces are known to occur.[9,10] The gray-filled circle stands for the critical point for interfacial SiO$_2$ to decompose to SiO.[10] The (T, P_{O_2}) boundaries predicted in Fig. 4(a) for the decomposition of interfacial silica is consistent with experiments.

Compared to Si-HfO$_2$, the Pt-HfO$_2$ interface displays a smoother transition from one level of O coverage to another, especially for $\theta_O < 1$ [Fig. 5(a)]. Also, this interface can be oxidized only at a very high oxygen pressure and low temperature. In the UHV environment, the stable interfacial O coverage between Pt and HfO$_2$ is 0.5–1 ML. In view that experimental data for the Pt-HfO$_2$ interface morphologies is sparse, we compared our phase diagram with experimental data for Pt surface oxidation. In order to facilitate such a comparison, we make the following observation. Since 0.5 ML O at the Pt-HfO$_2$ interface passivates HfO$_2$ and has little interaction with Pt, the net interfacial O strongly bonded to Pt is actually $\theta_O - 0.5$ ML. Within this context, the interfacial Pt in Pt:0.5:HfO$_2$ behaves like a clean Pt surface. The open and solid squares in Fig. 5(a) stand for the (T, P_{O_2}) conditions at which 0.25 ML O-adsorbed (111) Pt and clean (111) Pt surfaces are observed in experiment, respectively, consistent with our $\theta_O - 0.5$ ML values of ~ 0.25 and 0, respectively, under those same conditions. Another interesting finding of this work is that the oxidation of Pt at the interface is similar to that of a free (111) Pt surface. The saturation coverage of the chemically adsorbed O on (111) Pt surface is 0.25–0.3 ML, after which a layer of PtO$_2$ forms immediately on the surface.[34] Here, we find that the corresponding $\theta_O - 0.5$ ML value beyond which interfacial PtO$_2$ is formed is 0.25–0.5.

C. Impact of other factors (e.g., the vibrational and configurational energy contributions) on interface phase diagrams

Despite the fact that electronic devices have entered the nanoscale regime, direct simulation of the entire gate stack with complete fidelity is still not practical. It has thus become inevitable to make several simplifying assumptions to make the calculations tractable. These include assumptions
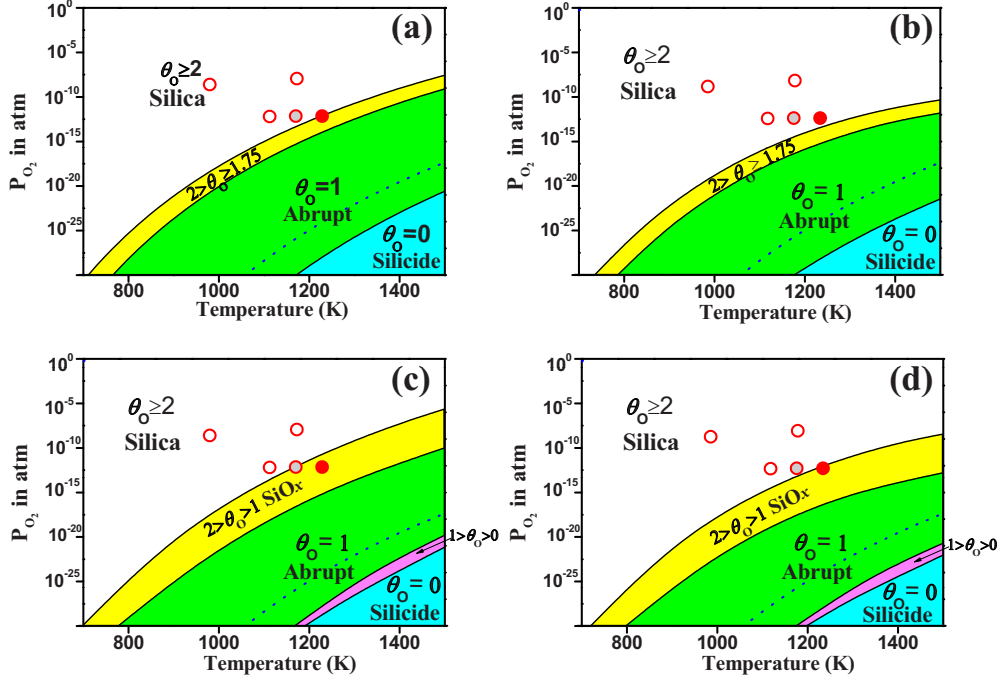
FIG. 4. (Color online) (a) The interface phase diagrams for the Si-HfO$_2$ interface, determined using Eq. (10), i.e., after neglecting the vibrational and configurational entropic contributions of the condensed phases to the relative interface free energy. (b) Same as (a), but with the vibrational entropic contribution ($\Delta F_{\theta_O}^v$) included. (c) Same as (a), but with the configurational entropic contribution ($\Delta F_{\theta_O}^c$) included. (d) The interface phase diagrams determined using Eq. (9); this is the same as (a), but with both the vibrational and configurational entropic contributions included. The solid curves indicate the interface phase boundaries and the dotted curves represent the onset of formation of bulk SiO$_2$. The open and solid circles stand for the condition to form SiO$_2$ and SiO at the Si-HfO$_2$ interfaces in experiments, respectively (Refs. 9 and 10). The gray-filled circle stands for the critical point for interfacial SiO$_2$ to decompose to SiO (Ref. 10).

dealing with the atomic level models and those dealing with the theory used. Included in the former class are constraints imposed by periodicity and coherency (which result in artificial strains on the heterostructures), and consideration of only a crystalline environment. We have commented on these factors earlier in this paper, and believe that the dominant "chemical" effects are indeed captured by our treatment. In particular, the impact of strain was directly addressed in Sec. III A, where it was shown that the relative interface energy (which determines the phase diagram) is insensitive to the strain built into our calculations.

Next, we address theoretical aspects left unexplored in the treatment above, e.g., the neglect of $\Delta F_{\theta_O}^v$ and $\Delta F_{\theta_O}^c$ [which allowed us to simplify Eqs. (9) and (10)]. To estimate $\Delta F_{\theta_O}^v$, we determined the vibrational DOS, $\sigma_{\theta_O}(w)$, for an interface with a certain O coverage and frequency w through harmonic normal mode analysis by allowing only the interfacial O, Si, Pt, or Hf atoms, as appropriate, to vibrate (i.e., all the O atoms that define the interfacial coverage and the other atoms closest to the interfacial plane). The vibrational contribution to the free energy [to be used in Eq. (9)] is then given by

$$F_{\theta_O}^v = \int [\hbar w/2 + kT \ln(1 - e^{-\hbar w/kT})]\sigma_{\theta_O}(w)dw. \quad (11)$$

The vibration of atoms away from the interface for θ_O and 0.5 are expected to be roughly equivalent and are assumed to cancel out in the computation of $\Delta F_{\theta_O}^v$. This analysis was

performed for all the interfaces considered. However, for clarity, we show $\Delta F_{\theta_O}^v/A$ for θ_O values of only 0 and 2 in Fig. 6 as these two extreme coverages provide an idea of the magnitude of the vibrational energy contribution. The roughly flat region at low temperatures is due to zero-point vibrations [first term of Eq. (11)]. The temperature-dependent (second) term of Eq. (11) contributes to a decrease (increase) in $\Delta F_{\theta_O}^v$ with increasing temperature for θ_O values larger (smaller) than 0.5, and in all cases going through zero above 500 K. This has the implication that lower (higher) values of the O coverages are favored at lower (higher) temperatures, with the vibrational entropic contribution having negligible impact in an intermediate temperature range when $\Delta F_{\theta_O}^v$ goes through zero. Features that reflect these expectations indeed manifest in the phase diagrams of Figs. 4(b) and 5(b), which have been created for the Si-HfO$_2$ and Pt-HfO$_2$ interfaces with the explicit inclusion of $\Delta F_{\theta_O}^v$ in the determination of the interface free energy [i.e., Eq. (9) with $\Delta F_{\theta_O}^c$ =0]. It can be seen that the impact of including $\Delta F_{\theta_O}^v$ results in rather minor changes to the features of the phase diagrams (most notably, the enlargement of the $\theta_O \geq 2$ phase region at high temperatures in the Si-HfO$_2$ interface phase diagram, and a shrinking of this region at low temperatures in the Pt-HfO$_2$ interface phase diagram). While this analysis provides a justification for the neglect of the vibrational contribution in prior treatments, we note that systems involving lighter atoms, e.g., H, may require explicit inclusion of the vibrational contribution to the free energy.
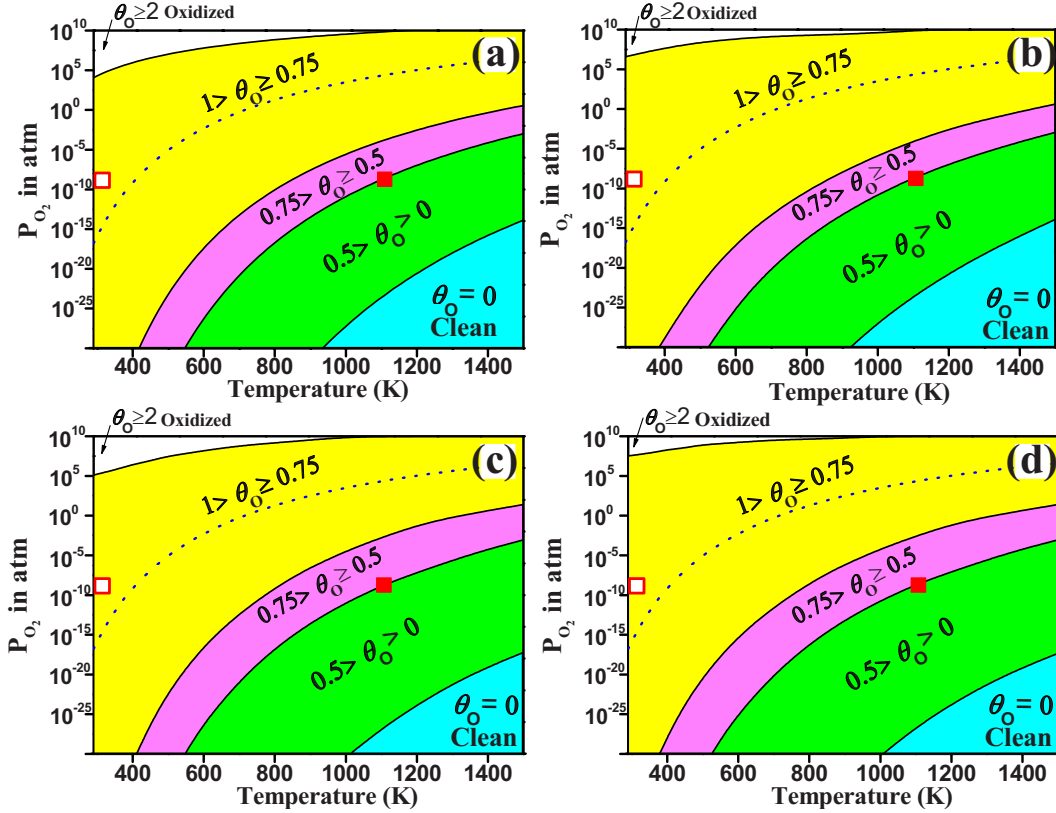
FIG. 5. (Color online) (a) The interface phase diagrams for the Pt-HfO$_2$ interface, determined using Eq. (10), i.e., after neglecting the vibrational and configurational entropic contributions of the condensed phases to the relative interface free energy. (b) Same as (a), but with the vibrational entropic contribution ($\Delta F_{\theta_O}^v$) included. (c) Same as (a), but with the configurational entropic contribution ($\Delta F_{\theta_O}^c$) included. (d) The interface phase diagrams determined using Eq. (9); this is the same as (a), but with both the vibrational and configurational entropic contributions included. The solid curves indicate the interface phase boundaries and the dotted curves represent the onset of formation of bulk PtO$_2$. The open and solid squares are the T and P_{O_2} when a 0.25 ML O-adsorbed (111) Pt surface and a clean (111) Pt surface were observed, respectively (Ref. 34).

Finally, we estimate the impact of $\Delta F_{\theta_O}^c$ on the interface phase diagram by assuming that the O atom sites for $\theta_O \in [0,1]$ are equivalent and O atom sites penetrating X layers are energetically identical. We note that this assumption constitutes an upper bound to the configurational entropy contribution, and is justified by the lack of dependence of the binding energy per O atom at the studied interfaces, as seen here (note, for instance, the linear behavior of Fig. 2) and elsewhere.[13] Thus, using Stirling's approximation, $F_{\theta_O}^c$ may be defined as follows. When $0 < \theta_O < 1$, $F_{\theta_O}^c = 4kT \times [\theta_O \ln \theta_O + (1-\theta_O)\ln(1-\theta_O)]$. When $1 < \theta_O < 2$, $F_{\theta_O}^c = 4kT \times [(\theta_O-1)\ln(\theta_O-1) + (2-\theta_O)\ln(2-\theta_O)]$. When $\theta_O = 0$, 1, and 2, $F_{\theta_O}^c = 0$. Figure 6 also shows the $\Delta F_{\theta_O}^c$ contribution for $\theta_O = 0$, 1, and 2. Unlike $\Delta F_{\theta_O}^v$, $\Delta F_{\theta_O}^c$ displays a steady rise with temperature. Moreover, as the variation in $\Delta F_{\theta_O}^c$ with θ_O is much smoother, inclusion of this contribution is expected to eliminate abrupt transitions between phases. Figures 4(c) and 5(c) show the Si-HfO$_2$ and Pt-HfO$_2$ interface phase diagrams when $\Delta F_{\theta_O}^c$ is explicitly included (but $\Delta F_{\theta_O}^v$ is not included) in the determination of the interface free energy [i.e., Eq. (9) with $\Delta F_{\theta_O}^v = 0$]. As expected, the inclusion of the configurational energy makes the transitions less abrupt and makes some intermediate interfacial phases appear in the

phase diagram, e.g., the $0 < \theta_O < 1$ and $1 < \theta_O < 1.75$ regions. We refer to $1 < \theta_O < 2$ as a "SiO$_x$" suboxide region and note that the presence of this phase region in the phase diagram brings our predictions for the formation and decomposition of interfacial silica more in line with experimental observations. In contrast to the Si-HfO$_2$ case, the interface phase diagrams with and without $\Delta F_{\theta_O}^c$ for Pt-HfO$_2$ are very similar to each other. The inclusion of $\Delta F_{\theta_O}^c$ causes only slight shifts to the phase boundaries and no new phase regions appear.

Figures 4(d) and 5(d) display the corresponding phase diagrams when both the vibrational and configurational energies are included in the treatment [i.e., when Eq. (9) is used]. Not surprisingly, simultaneous inclusion of these two contributions also does not result in significant differences with respect to the phase diagrams of Figs. 4(a) and 5(a). Nevertheless, these calculations provide an estimate of errors that may be introduced due to the neglect of such contributions.

We note that our phase diagrams are in favorable agreement with available experimental data. While such an agreement with experiments may be viewed as fortuitous, this may indicate that all the dominant contributions to the interface free energy have been included in this treatment [even at the level of Eq. (10)]. The unaddressed issues of deficiencies

TABLE II. $\Delta\mu'_{O_2}(T, P_0)$ computed based on tabulated JANAF data, constant C_p assumption and statistical thermodynamics. P_0 stands for 1 atm.

T (K)	$\Delta\mu'_{O_2}(T, P_0)$ (eV)		
	JANAF data	Constant C_p	Statistical thermo
300	−0.548	−0.546	−0.548
400	−0.765	−0.763	−0.766
500	−0.991	−0.987	−0.992
600	−1.222	−1.217	−1.224
700	−1.460	−1.453	−1.461
800	−1.702	−1.693	−1.704
900	−1.949	−1.936	−1.950
1000	−2.199	−2.183	−2.201
1100	−2.453	−2.433	−2.455
1200	−2.711	−2.686	−2.713
1300	−2.972	−2.942	−2.974
1400	−3.235	−3.199	−3.237
1500	−3.501	−3.459	−3.503

FIG. 6. (Color online) The vibrational and configurational contributions (i.e., $\Delta F^v_{\theta_O}/A$ and $\Delta F^c_{\theta_O}/A$, respectively) to the relative interface free energy, $\Delta\gamma_{\theta_O}$ [defined in Eq. (9)], as a function of temperature for the Si-HfO$_2$ and Pt-HfO$_2$ interfaces. Results pertaining to θ_O values of 0 and 2 are shown for the vibrational contribution, and those for 0, 1, and 2 for the configurational contribution. By definition, the $\Delta F^c_{\theta_O}/A$ values are identical for the three coverages. The slight difference in the $\Delta F^c_{\theta_O}/A$ values for the Si-HfO$_2$ and Pt-HfO$_2$ interfaces are due to the difference in the interface area A for these two cases.

inherent to approximations within DFT are presumably unimportant in the class of systems studied here (or may have participated in a fortuitous cancellation of errors). We do note that FPT studies may benefit from (the relatively inexpensive) explicit inclusion of configurational entropic contributions to the free energy especially when a lack of such inclusion results in abrupt transitions between phases.

IV. SUMMARY

The interface stabilities of Si-HfO$_2$ and Pt-HfO$_2$ as a function of temperature and O$_2$ pressure have been investigated using first principles thermodynamics. Our results can be summarized as follows

(1) at UHV conditions, Si-HfO$_2$ would present a silicalike interface. Under the same conditions, the stable O coverage at Pt-HfO$_2$ interface is 0.5–1 ML.

(2) The oxidation of the Pt-HfO$_2$ interface is similar to that of a free (111) Pt surface. In both cases, there exists a saturation O coverage before rapid formation of surface/interfacial PtO$_2$ is favored.

(3) Neglecting vibrational ($\Delta F^v_{\theta_O}$) and configurational ($\Delta F^c_{\theta_O}$) contributions to the free energies of the condensed phases, as widely done in FPT studies, does not result in serious errors in the computed interface phase diagrams. Inclusion of $\Delta F^v_{\theta_O}$ in the treatment causes minor changes to the phase boundaries at high and low temperatures, and the inclusion of $\Delta F^c_{\theta_O}$ "smoothes" the transition between different phases by making some intermediate interfacial phases appear in the case of the Si-HfO$_2$ system.

(4) The computed interface phase diagrams for both the Si-HfO$_2$ and Pt-HfO$_2$ interfaces are consistent with previous experimental observations at various temperatures and pressures. These results are thus indicative of the predictive na-
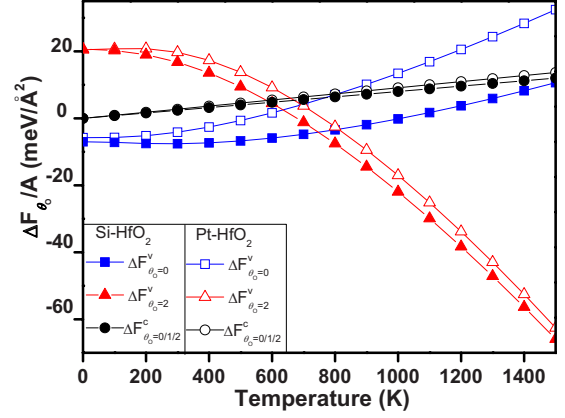
ture and usefulness of such first principles structure-processing relationship studies for the high-K gate stack classes of systems.

APPENDIX

For the specific case of O$_2$ gas, we summarize three widely used approaches adopted to capture the temperature (T) and pressure (P_{O_2}) dependence of the chemical potential of the gas phase species. The first two of these approaches[32,35] rely on the availability of empirical thermodynamic data [e.g., JANAF (Ref. 36)] and the last one, which uses statistical mechanics,[32,37] may be regarded as a purely *ab initio* approach.

1. Tabulated JANAF data

A useful definition for the chemical potential of O$_2$, $\mu_{O_2}(T, P_{O_2})$, is[38]

$$\begin{aligned} \mu_{O_2}(T, P_{O_2}) &= E^{DFT}_{O_2} + \Delta\mu_{O_2}(T, P_{O_2}) \\ &= E^{DFT}_{O_2} + E^{ZPE}_{O_2} + \Delta\mu'_{O_2}(T, P_0) + kT\ln(P_{O_2}/P_0), \end{aligned}$$

(A1)

where $E_{O_2}^{DFT}$ and $E_{O_2}^{ZPE}$ are the DFT energy and the zero-point vibrational energy of an isolated O_2 molecule at 0 K. The second equality of the above equation defines $\Delta\mu_{O_2}(T, P_{O_2})$, and $\Delta\mu'_{O_2}(T, P_0)$ is the difference in the chemical potentials of O_2 at $(0\ \text{K}, P_0)$ and at (T, P_0), where P_0 stands for the reference pressure, taken generally to be 1 atm. $\Delta\mu'_{O_2}(T, P_0)$ in Eq. (A1) can be expressed as

$$\Delta\mu'_{O_2}(T, P_0) = \Delta H(T, P_0) - TS(T, P_0), \quad \text{(A2)}$$

where $\Delta H(T, P_0)$ and $S(T, P_0)$ are the enthalpy and entropy of O_2 at T and P_0 with respect to the values at 0 K. These two values can be obtained from the JANAF thermochemical tables. The computed $\Delta\mu'_{O_2}(T, P_0)$ based on this method for a set of temperatures is listed in the second column in Table II. The last term in Eq. (A1) accounts for pressure values different from P_0.

2. Constant C_p assumption

Within this second approach, $\Delta\mu'_{O_2}(T, P_0)$ is computed by assuming that the specific heat at constant pressure, C_p, is $3.5k$ for $T \geq 298$ K. Furthermore, tabulated values of the standard ($T_0 = 298$ K, $P_0 = 1$ atm) enthalpy $H_0 = 9.02 \times 10^{-2}$ eV and entropy $S_0 = 2.12 \times 10^{-3}$ eV/K (Ref. 35) are also used. In terms of C_p, H_0, and S_0, $\Delta\mu'_{O_2}(T, P_0)$ can be written as

$$\Delta\mu'_{O_2}(T, P_0) = H_0 + C_p(T - T_0) - T[S_0 + C_p \ln(T/T_0)]. \quad \text{(A3)}$$

From Eqs. (A1) and (A3), one can determine $\mu_{O_2}(T, P_{O_2})$. It should be noted that the assumption underlying the specific choice of the C_p value of $3.5k$ is that only translational and rotational degrees of freedom of the O_2 molecule are excited. Since the characteristic T for the excitation of the vibrational degrees of freedom is very high (≈ 2230 K, see below), $\mu_{O_2}(T, P_{O_2})$ computed using this approach is expected to be accurate up to such high temperatures. The third column of Table II lists $\Delta\mu'_{O_2}(T, P_0)$ computed in this way.

3. Statistical thermodynamics

$\mu_{O_2}(T, P_{O_2})$ can also be calculated *ab initio* based on statistical thermodynamics and DFT determination of bond lengths, vibrational frequencies, and total energies. Within the framework of statistical mechanics, the chemical potential of O_2 can be computed based on the following equation:[37]

$$\mu_{O_2}(T, P_{O_2}) = G(T, P_{O_2})/N$$
$$= \left(-kT \ln Z + V\left[\frac{\partial(kT \ln Z)}{\partial V} \right]_T \right)/N, \quad \text{(A4)}$$

where $G(T, P_{O_2})$ is the Gibbs free energy of a system containing N O_2 molecules with V being the corresponding volume. Z stands for the partition function and equals

$$Z = (z_t z_r z_v z_e)^N/N!, \quad \text{(A5)}$$

where z_t, z_r, z_v, and z_e are, respectively, the translational, rotational, vibrational, and electronic partition functions for one O_2 molecule. Using standard expressions for the molecular partition functions for an ideal diatomic molecule gas,[37] one obtains

$$\Delta\mu'_{O_2}(T, P_0) = kT \ln\frac{P_0}{(2\pi mkT/h^2)^{1.5}kT} - kT \ln\frac{T}{2\theta_r}$$
$$+ kT \ln(1 - e^{-\theta_v/T}) - kT \ln 3. \quad \text{(A6)}$$

The four terms in the right represent the translational, rotational, vibrational, and the electronic contributions, respectively. h and m are the Planck's constant and the mass of an O_2 molecule, respectively. θ_r and θ_v are the characteristic rotational and vibrational temperatures, respectively, which are calculated here (using the DFT bond length and vibrational frequency of the O_2 molecule) to be 1.99 K and 2238 K, consistent with the corresponding experimental values (2.07 and 2230 K).[37] The factor 3 in the last term accounts for the fact that one O_2 molecule has two unpaired electrons, and hence three different spin configurations, i.e., $\uparrow\uparrow$, $\downarrow\downarrow$, and $\uparrow\downarrow$. $\Delta\mu'_{O_2}(T, P_0)$ calculated using this *ab initio* prescription [Eq. (A6)] is tabulated in the last column of Table II.

It can be seen from Table II that the three approaches for computing $\Delta\mu'_{O_2}(T, P_0)$ display similar results. The slight deviation of the results of the constant C_p method from those of the other two at high temperatures is the result of the neglect of the vibrational contribution to the C_p.

---

*Present address: Fritz-Haber-Institut der Max-Planck-Gesellschaft, Faradayweg 4-6, D-14195 Berlin, Germany.

†rampi@ims.uconn.edu

[1] K. Reuter and M. Scheffler, Phys. Rev. Lett. **90**, 046103 (2003).

[2] R. B. Getman, W. F. Schneider, A. D. Smeltz, W. N. Delgass, and F. H. Ribeiro, Phys. Rev. Lett. **102**, 076101 (2009).

[3] R. Grau-Crespo, K. C. Smith, T. S. Fisher, N. H. de Leeuw, and U. V. Waghmare, Phys. Rev. B **80**, 174117 (2009).

[4] C. G. Van de Walle and J. Neugebauer, Phys. Rev. Lett. **88**, 066103 (2002).

[5] R. M. Wallace and G. D. Wilk, Crit. Rev. Solid State Mater. Sci. **28**, 231 (2003).

[6] M. Wu, Y. I. Alivov, and H. Morkoc, J. Mater. Sci.: Mater. Electron. **19**, 915 (2008).

[7] X. Y. Qiu, H. W. Liu, F. Fang, M. J. Ha, and J. M. Liu, Appl. Phys. Lett. **88**, 072906 (2006).

[8] E. J. Preisler, S. Guha, M. Copel, N. A. Bojarczuk, M. C. Reuter, and E. Gusev, Appl. Phys. Lett. **85**, 6230 (2004).

[9] S. J. Wang, P. C. Lim, A. C. H. Huan, C. L. Liu, J. W. Chai, S. Y. Chow, and J. S. Pan, Appl. Phys. Lett. **82**, 2047 (2003); M. Copel, M. C. Reuter, and P. Jamison, *ibid.* **85**, 458 (2004).

[10] N. Miyata, T. Nabatame, T. Horikawa, M. Ichikawa, and A.

Toriumi, Appl. Phys. Lett. **82**, 3880 (2003).

[11] C. Tang, B. Tuttle, and R. Ramprasad, Phys. Rev. B **76**, 073306 (2007).

[12] C. Tang and R. Ramprasad, Phys. Rev. B **75**, 241302(R) (2007).

[13] C. Tang and R. Ramprasad, Appl. Phys. Lett. **92**, 182908 (2008).

[14] M. H. Hakala, A. S. Foster, J. L. Gavartin, P. Havu, M. J. Puska, and R. M. Nieminen, J. Appl. Phys. **100**, 043708 (2006).

[15] P. Broqvist and A. Pasquarello, Microelectron. Eng. **84**, 2022 (2007).

[16] D.-Y. Cho, K.-S. Park, B.-H. Choi, S.-J. Oh, Y. J. Chang, D. H. Kim, T. W. Noh, R. Jung, and J.-C. Lee, Appl. Phys. Lett. **86**, 041913 (2005).

[17] H. Y. Yu, C. Ren, Y.-C. Yeo, J. F. Kang, X. P. Wang, H. H. H. Ma, M.-F. Li, D. S. H. Chan, and D.-L. Kwong, IEEE Electron Device Lett. **25**, 337 (2004).

[18] J. K. Schaeffer, L. R. C. Fonseca, S. B. Samavedam, Y. Liang, P. J. Tobin, and B. E. White, Appl. Phys. Lett. **85**, 1826 (2004).

[19] J. K. Schaeffer, S. Samavedam, L. Fonseca, C. Capasso, O. Adetutu, D. Gilmer, C. Hobbs, E. Lckowski, R. Gregory, Z. X. Jiang, Y. Liang, K. Moore, D. Roan, B. Y. Nguyen, P. Tobin, and B. White, Mat. Res. Soc. Symp. Proc. No. 811, D4.1.1 (2004).

[20] J. Robertson, O. Sharia, and A. A. Demkov, Appl. Phys. Lett. **91**, 132912 (2007).

[21] N. Miyata, Y. Morita, T. Horikawa, T. Nabatame, M. Ichikawa, and A. Toriumi, Phys. Rev. B **71**, 233302 (2005).

[22] G. Kresse and J. Furthmuller, Phys. Rev. B **54**, 11169 (1996).

[23] J. P. Perdew, J. A. Chevary, S. H. Vosko, K. A. Jackson, M. R. Pederson, D. J. Singh, and C. Fiolhais, Phys. Rev. B **46**, 6671 (1992).

[24] D. Vanderbilt, Phys. Rev. B **41**, 7892 (1990).

[25] P. E. Blöchl, Phys. Rev. B **50**, 17953 (1994); G. Kresse and D. Joubert, *ibid.* **59**, 1758 (1999).

[26] C. Tang and R. Ramprasad, Phys. Rev. B **81**, 161201(R) (2010).

[27] J. Adam and M. D. Rodgers, Acta Crystallogr. **12**, 951 (1959).

[28] C. R. Hubbard, H. E. Swanson, and F. A. Mauer, J. Appl. Crystallogr. **8**, 45 (1975).

[29] W. G. Ralph, *Wyckoff, The Structure of Crystals* (Reinhold, New York, 1935), p. 11.

[30] P. W. Peacock and J. Robertson, Phys. Rev. Lett. **92**, 057601 (2004).

[31] A. V. Gavrikov, A. A. Knizhnik, A. A. Bagatur'yants, B. V. Potapkin, L. R. C. Fonseca, M. W. Stoker, and J. Schaeffer, J. Appl. Phys. **101**, 014310 (2007).

[32] K. Reuter and M. Scheffler, Phys. Rev. B **65**, 035406 (2001).

[33] K. Reuter and M. Scheffler, Phys. Rev. B **68**, 045407 (2003).

[34] U. Engström and R. Ryberg, Phys. Rev. Lett. **82**, 2741 (1999).

[35] J. Osorio-Guillén, S. Lany, S. V. Barabash, and A. Zunger, Phys. Rev. Lett. **96**, 107203 (2006).

[36] D. R. Stull and H. Prophet, *JANAF Thermochemical Tables*, Natl. Bur. Stand. Ref. Data Ser., Natl. Bur. Stand. (U.S.) Circ. No. 37, 2nd ed. (U.S. GPO, Washington, D.C., 1971).

[37] T. L. Hill, *Introduction to Statistical Thermodynamics* (Dover, New York, 1986); L. K. Nash, *Elements of Statistical Thermodynamics* (Addison-Wesley, Reading, MA, 1972).

[38] D. Sholl and J. A. Steckel, *Density Functional Theory: A Practical Introduction* (Wiley, Hoboken, NJ, 2009).